

Magnetic Nanodevices and Spin-Transport Properties of a Two-Dimensional CrSCl Monolayer

Juncai Chen¹, Yongliang Guo^{1,2}, Chunlan Ma,^{3,†} Shijing Gong,⁴ Chuanxi Zhao^{1,5}, Tianxing Wang,¹ Xiao Dong,¹ Zhaoyong Jiao,¹ Shuhong Ma,¹ Guoliang Xu^{1,1}, and Yipeng An^{1,*}

¹ School of Physics, Henan Normal University, Xinxiang 453007, China

² School of Science, Henan Institute of Technology, Xinxiang 453003, China

³ School of Physics and Technology, Suzhou University of Science and Technology, Suzhou 215009, China

⁴ Department of Physics, East China Normal University, Shanghai 200062, China

⁵ Siyuan Laboratory, Guangdong Provincial Engineering Technology Research Center of Vacuum Coating Technologies and New Energy Materials, Department of Physics, Jinan University, Guangzhou 510632, China

(Received 1 December 2022; revised 26 February 2023; accepted 4 April 2023; published 3 May 2023)

The two-dimensional intrinsic ferromagnet CrSCl monolayer has considerable potential for application in the development of spintronic devices because of properties such as robust ferromagnetic ordering, large spin polarization, high Curie temperature, and high carrier mobilities. Here, we investigate the electromagnetic properties of the CrSCl monolayer and the spin-transport properties of some conceptual magnetic devices we construct, such as *p-n*-junction diodes, field-effect transistors, and phototransistors, by means of first-principles calculations. The results indicate that the *p-n*-junction diodes of the CrSCl monolayer exhibit full spin-polarized transport behavior, and both the *p-n* and *p-i-n* junctions show excellent spin-filtering behavior. The phototransistor of the CrSCl monolayer exhibits spin-resolved photoresponse characteristics for different wavelengths of light. Furthermore, it possesses the ability to generate a fully spin-up polarized current in the visible range. Our results provide key insights into the fundamental physical properties and the underlying transport and photoresponse mechanisms of the CrSCl monolayer.

DOI: 10.1103/PhysRevApplied.19.054013

I. INTRODUCTION

Two-dimensional (2D) materials have gained significant attention in recent years, owing to their unusual physical properties in which both charge and heat transport are confined to a plane. They have considerable prospects for diverse applications, such as electronics [1–4], optoelectronics [5,6], sensors [7], spintronics [8], and field-effect transistors [9,10]. Constant efforts toward reducing the size of devices include developing low-dimensional materials with exceptional properties, such as robust ferromagnetic (FM) ordering, large spin polarization, and high Curie temperature for next-generation nanospintronic devices [11]. Because traditional 2D materials, such as graphene [12], boron nitride [13], and black phosphorus [14], are intrinsically nonmagnetic, their applications in the field of spintronics are trapped.

2D intrinsic FM materials are now being extensively used to develop magnetic nanodevices as well as for spintronic applications [15–17]. Recent studies using magneto-optical Kerr effect microscopy indicate that monolayer chromium triiodide (CrI_3) exhibits a Curie temperature of 45 K and possesses FM properties [18]. This has further stimulated the exploration and investigation of 2D FM materials and increased the potential of designing various spintronic devices. Subsequently, 2D magnetic monolayers of VSe_2 [19,20], $\text{Cr}_2\text{Ge}_2\text{Te}_6$ [21–23], Fe_3GeTe_2 [24–26], and MnBi_2Te_4 [27–30], which also exhibit intrinsic FM and have various fascinating physical properties, have been discovered, fabricated, and investigated extensively; some of them show great potential for applications in spintronic devices [24,26,30]. Importantly, these materials have intrinsic FM ordering with a large magnetic moment above room temperature, making them attractive for spintronics applications and the development of magnetic nanodevices. Strikingly, theoretical studies on monolayer chromium chalcogenide halides, CrXY ($X = \text{O}, \text{S}, \text{Se}, \text{Te}; Y = \text{F}, \text{Cl}, \text{Br}, \text{I}$) [31–34], show that they possess robust FM ordering with high spin polarization and a high Curie temperature. Furthermore,

*ypan@htu.edu.cn

†wlxmcl@mail.usts.edu.cn

the van der Waals (vdW) bulk compounds, which crystallize in orthorhombic structures, stacked with CrXY's isostructural 2D monolayers have been widely studied since the 1970s [35,36]. More recently, the stable antiferromagnetic vdW bulk materials CrOCl [37,38] and CrSBr [39] were synthesized using the chemical-vapor-transport method. Guo *et al.* [40] predicted that the cleavage energies of the CrSY materials were about 0.16, 0.21, and 0.25 J m⁻² for CrScI, CrSBr, and CrSI, respectively, using density-functional theory (DFT); these values are smaller than that of graphene [(0.32 ± 0.03) J m⁻²] [41], indicating that monolayer CrSX is relatively easy to obtain from the corresponding bulk material by mechanical exfoliation. Especially, among CrXY materials, the CrScI monolayer is a FM semiconductor with a high hole mobility of up to 6.6×10^3 cm² V⁻¹ S⁻¹ and a high Curie temperature of up to 500 K [32]. Furthermore, it exhibits excellent dynamic and thermal stability and requires a small exfoliation energy from the bulk [32,33,40]. Thus, it can be potentially used in next-generation spintronic and electronic devices.

Although the CrScI monolayer possesses excellent features, the fundamental behavior and the underlying mechanisms in device architectures, such as spin-polarized transport behavior, field-effect behavior, and photoreponse characteristics, have not been revealed. Here, we investigate the electromagnetic properties of the CrScI monolayer and the spin-transport properties of some conceptual magnetic devices we construct, such as *p-n*-junction diodes, field-effect transistors, and phototransistors, within the spin-polarized DFT framework combined with the nonequilibrium Green function method (NEGF) [42–44]. The rest of this paper is organized as follows. Section II presents the computational details. Section III contains the results and discussion, followed by a summary of this work in Sec. IV.

II. CALCULATION METHODS

Here, we focus on the CrScI monolayer and the spin-transport properties of several conceptual nanodevices, such as *p-n*-junction diodes, field-effect transistors, and phototransistors. All calculations are performed within the spin-polarized DFT NEGF method, as implemented in the Atomistix Toolkit code [42–44]. The spin-polarized generalized gradient approximation (GGA) combined with the Perdew-Burke-Ernzerhof (PBE) functional [45] is adopted to describe the exchange-correlation interactions. Considering the strong correlation of the 3d electrons, spin-polarized PBE + *U* calculations are applied in this work as a correction to the PBE. The on-site Hubbard *U* is set to 3.0 eV for Cr, according to previous work on related systems [40,46–48]. The electron wave functions are expanded using the linear combinations of atomic orbitals (LCAO) basis sets with a real-space grid density mesh

cutoff of 160 hartree. The optimized norm-conserving Vanderbilt pseudopotentials [49] at the level of SG15 type [50] are employed to describe the core electrons. Electronic band structures are also evaluated using the PBE + *U* and hybrid (HSE06) functional [51] for the band-gap correction. The Brillouin zone (BZ) is sampled using a $10 \times 1 \times 200$ *k*-point mesh generated via the Monkhorst-Pack scheme [52] for electrodes of the CrScI monolayer device. Structural relaxation is considered to be converged when the residual forces on each atom are less than 0.001 eV/Å. Furthermore, the total energy-convergence threshold is set to be 10^{-6} eV.

The DFT NEGF method is implemented for electron-transport calculations in each device system. The device system can be divided into three regions: the left and right electrode regions and the central scattering region. Self-consistent electronic structures of the device system are described using the Kohn-Sham and Poisson equations. The electrode regions are described by solving a bulk problem for the fully periodic electrode cell. Between the electrode and the central region, a Dirichlet boundary condition is adopted. The initial density matrix is constructed by first performing a self-consistent bulk calculation of the central region, which can give a very good initial guess for the density matrix. The nonequilibrium electron distribution in the central region is given by the occupied eigenstates of the system, which can be determined by the NEGF method. The energy integral is evaluated through a complex contour integration that is divided into two parts: an integral over equilibrium states and an integral over nonequilibrium states. The former is calculated using a semicircular complex contour with integral lower bound of 3.679 hartree and 30 circle points. The latter is performed along the real axis with a point density of 0.001 hartree.

To calculate the excited-state properties, the Heisenberg exchange Hamiltonian is calculated, which is given by [53]

$$H = - \sum_{i \neq j} J_{ij} \mathbf{e}_i \mathbf{e}_j, \quad (1)$$

where J_{ij} is the Heisenberg exchange-coupling constant between two particular sites (*i, j*); \mathbf{e}_i and \mathbf{e}_j are the normalized local spin vectors on atoms *i* and *j*. Note that the present work is focused on the case of the magnetic isotropic Hamiltonian, and the contribution from magnetic anisotropy is not included in this formula. The spin-wave energy, $E(\mathbf{q})$, is related to the exchange parameters, J_{ij} , by a Fourier transformation:

$$E(\mathbf{q}) = \frac{4\mu_B}{M} \sum_{j \neq 0} J_{0j} (1 - \exp[i\mathbf{q} \cdot \mathbf{R}_{0j}]), \quad (2)$$

where $\mathbf{R}_{0j} = \mathbf{R}_0 - \mathbf{R}_j$ is the lattice vector in real space, \mathbf{q} is a vector in the corresponding Brillouin zone, *M* is the magnetic moment per atom, and μ_B is the Bohr magneton.

The Curie temperature of a ferromagnet can be estimated from the Heisenberg model based on the random phase approximation (RPA) [53]:

$$\frac{1}{k_B T_C} = \frac{6\mu_B}{M} \frac{1}{N_q} \sum_q \frac{1}{E(\mathbf{q})}, \quad (3)$$

where N_q is the number of q points in the Brillouin zone. This method is well used to reproduce the theoretical Curie temperatures of some metals, which have good agreement with experimental results [53].

III. RESULTS AND DISCUSSION

A. Electronic and magnetic properties

The CrSCl monolayer has an orthorhombic structure [space group $Pmmn$, see Fig. 1(a)], wherein each Cr atom is coordinated by four S and two Cl atoms. Considering the FM ground spin state [40], we calculate the lattice parameters for the CrSCl monolayer crystal. Furthermore, a vacuum spacing of approximately 25 Å is added along the perpendicular direction to avoid interactions between adjacent layers. The current results and other previously reported values [40,54] are listed in Table I. From this table, it can be seen that our calculated lattice constants, a and b , are in excellent agreement with the previously reported values [40,54]. The calculated magnetic moment and nearest and next-nearest exchange-coupling constants,

J_1 and J_2 , respectively, along with those data previously reported [32,40], are also given in Table I. The magnetism mainly stems from the Cr atoms, which possess a large magnetic moment of $3.288\mu_B$ (PBE) and $3.478\mu_B$ (PBE + U). The net magnetic moment per formula unit is $3.004\mu_B$ for both PBE and PBE + U . The nearest (J_1) and next-nearest (J_2) exchange couplings in the CrSCl structure are shown in Fig. 1(a). The values of J_1 and J_2 are 5.84 and 7.82 meV, respectively, which are obtained with the PBE functional; these values are slightly larger than those reported in the literature [32,40]. Note that the results of the PBE + U calculations are closer to the references, i.e., the values of J_1 and J_2 are 3.79 and 4.19 meV, respectively. The value of J_1 is close to that reported in Ref. [40] (3.31 meV), and the value of J_2 is between those reported in Ref. [32] (2.58 meV) and Ref. [40] (6.85 meV). The strong and positive spin-exchange coupling results in robust long-range FM ordering and a high Curie temperature in the CrSCl monolayer. A Curie temperature of about 369 K (PBE) is expected according to the RPA, and this value is in agreement with the previously reported values of 500 K (PBE) and 340 K (GGA + U) [32]. Note that the corresponding PBE + U result we obtain is 147 K, which is in excellent agreement with the value (150 K) obtained by Guo *et al.* [40] using Monte Carlo simulations.

The atom-resolved electronic band structures and density of states (DOS) are calculated using the PBE

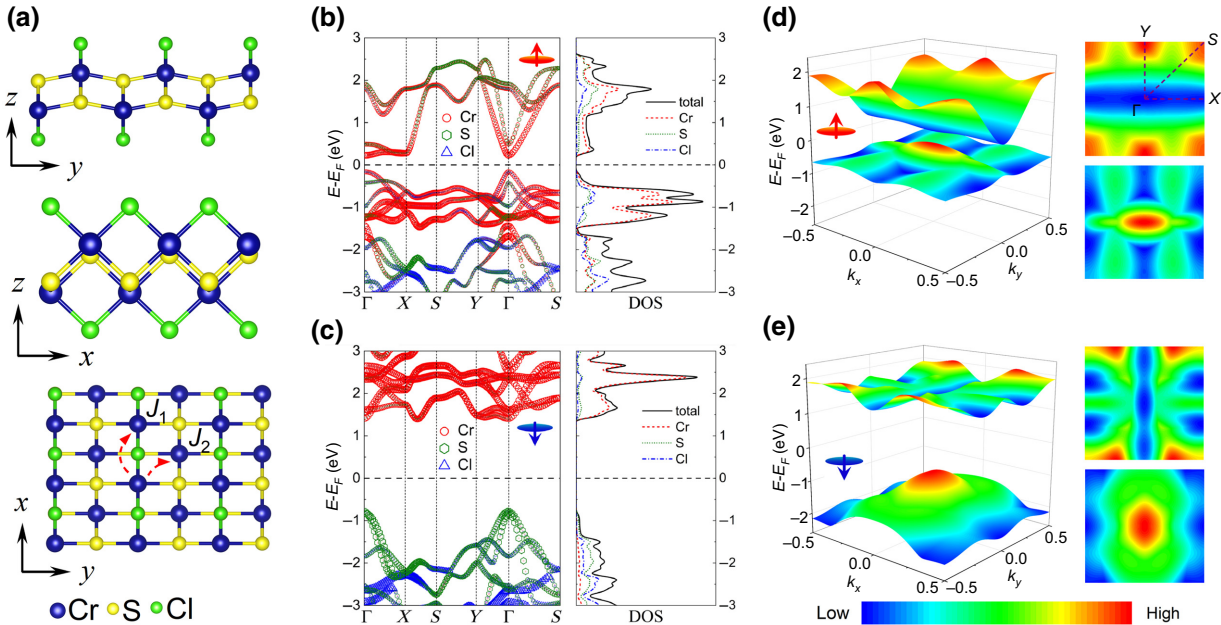


FIG. 1. Atomic and electronic structures of the 2D CrSCl monolayer. (a) Side (upper, middle) and top (bottom) views of the CrSCl monolayer crystal structure. J_1 and J_2 are the nearest and next-nearest exchange couplings, respectively. Element-projected electronic band and density of states for spin-up (b) and -down (c) states. 3D views of the top of the valence band and the bottom of the conduction band, and 2D projections in the first Brillouin zone for spin-up (d) and -down (e) states. Color map shows data for (d),(e) from low (blue) to high (red).

TABLE I. Optimized lattice constants (a and b), electronic band gap (E_g), magnetic moment (M), and nearest and next-nearest exchange-coupling constants (J_1 and J_2) for the CrSCl monolayer.

Lattice constants (Å)			$M (\mu_B)$		J (meV)	
a	b	E_g (eV)	M_{Cr}	M_{tot}	J_1	J_2
3.460 ^a	4.770 ^a	0.387 ^a	3.288 ^a	3.004 ^a	5.84 ^a	7.82 ^a
3.472 ^b	4.834 ^b	1.016 ^b	3.478 ^b	3.004 ^b	3.79 ^b	4.19 ^b
3.53 ^c	4.82 ^c	0.61 ^d	2.996 ^d		1.01 ^d	2.58 ^d
3.49 ^e	4.84 ^e	0.856 (PBE + U) ^e	3.15 ^e	2.90 ^e	3.31 ^e	6.85 ^e

^aPBE.

^bPBE + U .

^cRef. [54].

^dRef. [32].

^eRef. [40].

functional and are displayed in Figs. 1(b) and 1(c) for spin-up and –down states, respectively. For comparison, the electronic band structures are also calculated using the PBE + U and HSE06 functionals, as shown in Fig. S1 within the Supplemental Material [69]. The CrSCl monolayer is a semiconductor with a direct band gap of 0.387 (PBE); the values calculated using PBE + U and HSE06 functionals are 1.016 and 1.617 eV, respectively, which is consistent with the previously reported values of 1.86 eV (HSE06) [33], 0.61 eV (PBE) [32], and 0.856 eV (GGA + U) [40] to some extent. Note the small difference between our results and those reported in the literature may arise from the different methods, i.e., we use the LCAO basis sets for the expanded of electron wave functions, while those reported in the literature use the projected augmented wave method. Both the valence-band maximum (VBM) and conduction-band minimum (CBM) of the CrSCl monolayer are located at the Γ point, and the VBM is predominantly contributed to by orbitals of the S atoms, while the CBM is dominated by orbitals of the Cr atoms. Furthermore, the band structures in Figs. 1(b) and 1(c) demonstrate that the VBM and CBM are primarily contributed to by the spin-up electrons. The band gap of the spin-down states (2.179 eV) is significantly larger than that of the spin-up states (0.387 eV). These values indicate that the CrSCl monolayer can generate almost 100% spin-polarized carriers because the VB and CB near the Fermi level (E_F) are fully spin polarized. Therefore, this performance is ideal for the fabrication of spintronic devices with a strong spin-filtering effect. 3D views of the top of the valence band and the bottom of the conduction band, and 2D projections in the first Brillouin zone for spin-up and -down states are shown in Figs. 1(d) and 1(e). From Fig. 1(d), it can be seen that the band structure around the VBM and CBM exhibits a linear dispersion along the Γ -Y direction and is almost flat along the Γ -X direction for the spin-up states. These result in a small effective mass along the Γ -Y direction and a contrary value in the other direction, which is in agreement with the outcomes of

a previous report by Guo *et al.* [40], wherein it was shown that the effective masses along the Γ -Y direction were $0.078m_e$ (holes) and $0.421m_e$ (electrons), and those along the Γ -X direction were $4.017m_e$ for both holes and electrons (m_e is the free electron mass). The hole mobility of the CrSCl monolayer is further predicted to be $6.6 \times 10^3 \text{ cm}^2 \text{ V}^{-1} \text{ S}^{-1}$ along the Γ -Y direction [40].

The magnetic anisotropy energy (E_{MA}), which primarily originates from the spin-orbit coupling effects [55], is an important parameter for the spintronic applications of FM 2D materials, as it defines the stability of magnetization in a specific direction, according to the crystal lattice. Therefore, we examine the E_{MA} of the CrSCl monolayer using the force theorem [56], wherein the energy difference is evaluated using non-self-consistent band energies concerning the spin-orbit coupling:

$$E_{\text{MA}} = \sum_i f_i(\theta_1, \varphi_1) \epsilon_i(\theta_1, \varphi_1) - \sum_i f_i(\theta_0, \varphi_0) \epsilon_i(\theta_0, \varphi_0), \quad (4)$$

where $f_i(\theta, \varphi)$ is the occupation factor for band i (including both the band and k -point index) with spin orientation (θ, φ) , and $\epsilon_i(\theta, \varphi)$ is the corresponding band energy. The calculated results of angular dependence and orbital projection E_{MA} for the CrSCl monolayer are shown in Fig. 2. It is worth noting that both the in- and out-of-plane (corresponding to the x -y and y -z planes, respectively) energies are anisotropic. Furthermore, Fig. 2(a) indicates that the E_{MA} reaches its minimum when $\theta = 90^\circ$ in the y -z plane and $\varphi = 0^\circ$ in the x -y plane. This denotes that the easy-magnetization axis of the CrSCl monolayer is in plane and along the x direction, which is consistent with previous work [54]. Meanwhile, the E_{MA} has a strong dependency on both polar angles θ and φ , indicating strong magnetic anisotropy behavior of the CrSCl monolayer. In addition, the orbital projections of E_{MA} corresponding to the polar

angles of $(\theta = 90^\circ, \varphi = 90^\circ)$ and $(\theta = 90^\circ, \varphi = 0^\circ)$ are calculated as shown in Figs. 2(b) and 2(c). It is observed that the d_{xy} , d_{yz} , d_{xz} , $d_{x^2-y^2}$, and d_{z^2} orbitals of Cr mainly contribute to the E_{MA} at polar angles of $(\theta = 90^\circ, \varphi = 90^\circ)$, and all the d orbitals of Cr primarily determine the E_{MA} at polar angles of $(\theta = 90^\circ, \varphi = 0^\circ)$. Conversely, the contribution of other atoms of S and Cl to the E_{MA} is relatively small.

B. Transport behavior of the CrSCl monolayer in a p - n -junction diode

The CrSCl monolayer is expected to show good transport behavior along the y direction, as indicated in Fig. 1(a), because it has a smaller effective mass and relatively high carrier mobility along the Γ - Y direction. Therefore, a CrSCl monolayer p - n -junction diode [see Fig. 3(a)] is established using an electrostatic doping method with p - and n -type atom-compensation charges [57], and the y direction serves as the transmission direction. We investigate the transmission performance of the p - n -junction diodes under different doping concentrations, according to the typical doping concentration range of 10^{19} – 10^{21} cm^{-3} in the bulk [57,58]. The results show that the transmission performance of the CrSCl monolayer p - n -junction diode varies according to the doping concentration. A doping concentration that is either too high or too low is not conducive to improving the performance of the device. Here, we report only the results for three levels of doping densities of p - and n -type carriers, i.e., 7.5×10^{12} (low), 1.5×10^{13} (medium), and $3 \times 10^{13} \text{ cm}^{-2}$ (high), corresponding to 2.5×10^{19} , 5×10^{19} , and $1 \times 10^{20} \text{ cm}^{-3}$ in the bulk, respectively.

Each diode consists of the drain (D) and source (S) electrodes and the central scattering region (p - n junction). In transport calculations, a supercell of p - and n -doped CrSCl monolayer serves as the D and S electrodes, the length of which is semi-infinite along the direction of transmission. A positive current is generated from the D electrode to the S electrode when a forward D - S bias of V_b is applied and vice versa. The spin-resolved currents of the p - n -junction diode are calculated by [59]

$$I_\sigma(V_b) = \frac{e}{h} \int_{\mu_D}^{\mu_S} T^\sigma(E, V_b) [f_D(E - \mu_D) - f_S(E - \mu_S)] dE, \quad (5)$$

where σ represents the spin-up and -down states, and the total current I is the sum of I_σ . e is the electron charge and h is Planck's constant. $T^\sigma(E, V_b)$ is the spin-resolved transmission coefficient. $f_{D(S)} = \{1 + \exp[E - \mu_{D(S)}/k_B T_{D(S)}]\}^{-1}$ is the Fermi-Dirac distribution function of the $D(S)$ electrode with chemical potential $\mu_{D(S)}$ and temperature $T_{D(S)}$. The Fermi-Dirac distribution-function broadening is generally selected to be between 0.01 and 0.1 eV. We use the default value of 0.086 eV in QuantumATK throughout the

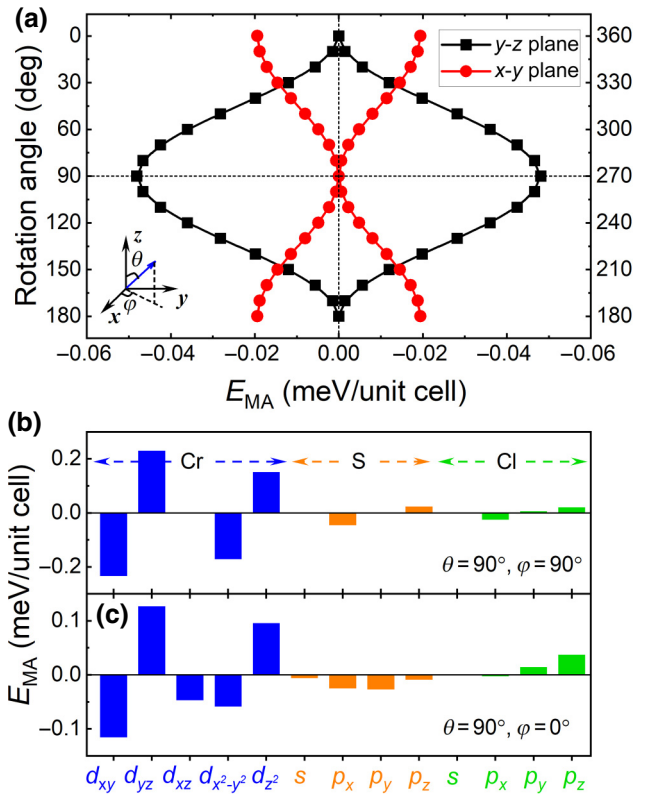


FIG. 2. E_{MA} of the CrSCl monolayer. (a) Variations of E_{MA} with polar angles θ and φ in the y - z and x - y planes. Inset shows polar coordinates. Orbital projections of E_{MA} corresponding to polar angles of (b) $\theta = 90^\circ, \varphi = 90^\circ$ (y direction) and (c) $\theta = 90^\circ, \varphi = 0^\circ$ (x direction). Energy of y ($\theta = 90^\circ, \varphi = 90^\circ$) and z ($\theta = 0^\circ, \varphi = 90^\circ$) directions are set as zero reference in x - y and y - z planes.

study, corresponding to 1000 K. The I - V curves calculated using the PBE functional for a high doping concentration are shown in Fig. 3(b), while those for low and medium doping concentrations are shown in Figs. S2(a) and S2(b) within the Supplemental Material [69], respectively. The current of the spin-up state is open at the negative-bias side with a low threshold voltage of $V_{on} = -0.1$ V (high), -0.2 V (medium), and -0.3 V (low). The maximum current density is about 4000 mA/mm at a bias of -0.5 V for a high doping concentration, which is approximately 8 times as high as that of the low doping concentration. In addition, a relatively small stationary current is generated for a bias above 0.3 V at the positive-bias side [see Figs. 3(b) and S2 within the Supplemental Material [69]]. The unidirectional transport feature can be described using the rectification ratio (R), which is given as $R = |I(-V_b)/I(V_b)|$. The maximum magnitude of the R of the p -junction diode is 10^4 , as shown in Fig. 3(b), and this value is much larger than that of the graphene|h-BN heterojunction [60] and close to that of the VS₂|MoS₂ heterojunction [8]. Furthermore, it displays an excellent spin-filtering effect, as

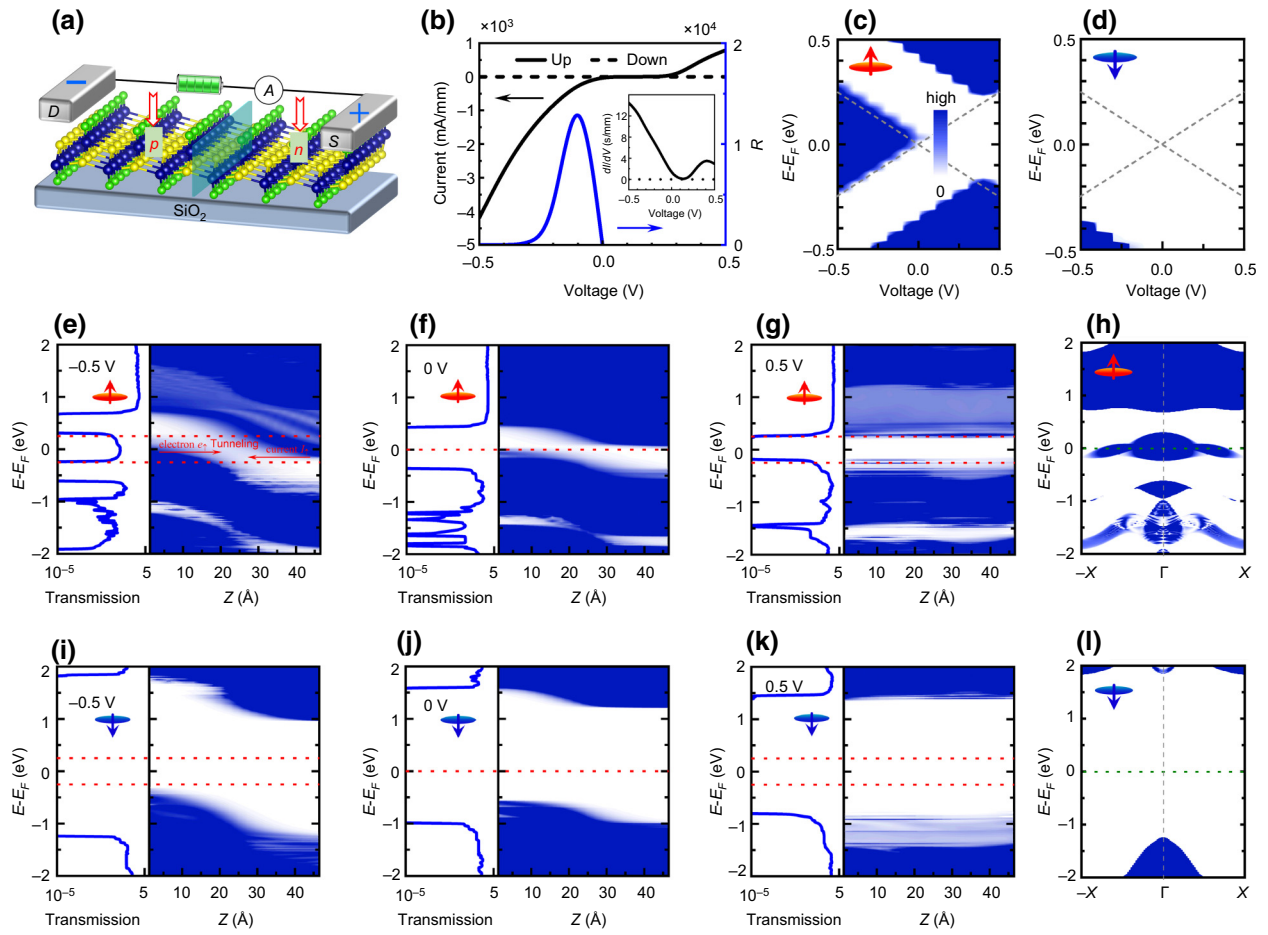


FIG. 3. Transport properties of the *p*-*n*-junction diode of the 2D CrScl monolayer for a doping concentration of $3 \times 10^{13} \text{ cm}^{-2}$. (a) Schematic of the *p*-*n*-junction diode of the CrScl monolayer. (b) Bias-dependent current and rectification ratio of the *p*-*n*-junction diode, with difference conductance curves shown in the inset. Transmission spectra of spin-up (c) and -down (d) states. Spin-resolved transmission coefficient, $T(E)$, and projected local density of states (PLDOS) under biases of -0.5 V (e),(i), 0 V (f),(j), and 0.5 V (g),(h). k -Dependent transmission coefficients, $T(E, k)$, at -0.5 V of spin-up (h) and -down (l) states. Color map shows data for (c)–(l) from 0 (white) to high (blue).

the current of the spin-down state is extremely close to zero over the entire bias range and when the polarization ratio, defined as $P = (I_{\uparrow} - I_{\downarrow})/(I_{\uparrow} + I_{\downarrow})$, almost equals 100% over the entire range. Actually, this character is also found in other materials, such as the transition-metal dichalcogenides WS₂ [61] and WSe₂ [62,63], as all of them have only one spin-state type around the Fermi level. The differential conductance (dI/dV) density of the spin-up state is approximately 14.5 S/mm at -0.5 V for a high-doping-concentration *p*-*n*-junction diode, as shown in the inset of Fig. 3(b). Furthermore, it can be seen that the dI/dV curve of the spin-down state almost equals zero over the entire bias range, and it also exhibits full spin-polarized behavior. For comparison, we investigate the bias-dependent current, rectification ratio, and difference conductance using PBE + U , as shown in Fig. S3(a) within the Supplemental Material [69], which shows a similar trend to that of the

results obtained using PBE. These excellent traits of the CrScl monolayer *p*-*n*-junction diode are ideal for use in nanodevices.

To further analyze the reasons why the CrScl monolayer *p*-*n*-junction diode possesses strong spin polarizability and good transmission properties, the spin-resolved transmission spectra, $T(E, V)$; transmission coefficients, $T(E)$; PLDOS; and k -dependent transmission coefficients, $T(E, k)$, for a high doping concentration are calculated, as shown in Figs. 3(c)–3(l). Meanwhile, those for low and medium doping concentrations are shown in Figs. S4–S6 within the Supplemental Material [69]. These transmission parameters indicate that the electrons of the spin-down state can barely transport in the *p*-*n*-junction diode, and, as a result, the diode possesses a strong spin polarizability. The electrons in the spin-up state can be easily transmitted for negative biases with large transmission coefficients

within the bias window (BW) [see Fig. 3(c)]. A few electrons can be transmitted under a positive bias of 0.4–0.5 V because of the smaller transmission coefficients in this bias region. From the PLDOS in Fig. 3, it can be seen that the bands of the *p*- and *n*-doped terminals shift up and down, respectively, when a negative bias is applied across the *p-n* junction and vice versa. A relatively high number of electron states enter the BW within the negative-bias region compared with the PLDOS under zero bias, thus driving a strong electron transmission under a negative bias, such as –0.5 V [see Fig. 3(e)]. Furthermore, some valence bands enter the BW under a bias of 0.5 V [see Fig. 3(g)], thereby generating a small transmission current under this condition. In addition, Figs. 3(h) and 3(l) show that the *k*-dependent transmission coefficients, $T(E, k)$, remain high over the whole Brillouin zone from Γ to X ($-X$) for the spin-up state. In contrast, $T(E, k)$ almost equals zero over the entire Brillouin zone for the spin-down state. This is the primary contributing factor to the robust spin polarization. For the low- and medium-doping-concentration *p-n*-junction diode, similar transition behavior can be observed to that in the high doping concentration. CrSCl is a primary candidate material for spin-filtering nanodevices.

C. Field-effect behaviors of the CrSCl monolayer *p-i-n*-junction transistor

The vertical electric field can also improve the transmission performance of a device. Therefore, we construct the *p-i-n*-junction field-effect transistors [FETs, see Fig. 4(a)] using the CrSCl monolayer and study their spin-dependent field-effect properties. The *p*- and *n*-doped CrSCl monolayer ($3 \times 10^{13} \text{ cm}^{-2}$) is used as electrodes on both sides of the FET, and the intrinsic CrSCl monolayer is used in the central intrinsic region (*i*) as the FET channel ($\sim 3 \text{ nm}$). The top and bottom gates are placed near the central intrinsic region, and they cover the entire region. The spin-resolved electron current through the *p-i-n*-junction FET is obtained by

$$I_\sigma(V_b, V_g) = \frac{e}{h} \int_{\mu_D}^{\mu_S} T^\sigma(E, V_b, V_g) [f_D(E - \mu_D) - f_S(E - \mu_S)] dE. \quad (6)$$

The spin-resolved *I-V* curves of the *p-i-n*-junction FET under gate voltages of 0, 5, and 10 V are shown in Fig. 4(b). The current density of the *p-i-n*-junction FET under zero gate voltage is slightly smaller than that of the *p-n*-junction diode with the same doping concentration because of the semiconducting nature of the central intrinsic region. Nevertheless, the *p-i-n*-junction FET shows the same spin-filtering behavior as the *p-n*-junction diode of the CrSCl monolayer. Furthermore, the current density is

dramatically increased at the negative-bias side as the gate voltage is applied, while a contrasting trend is observed at the positive-bias side. The forward current can be almost ignored under a gate voltage of 10 V, as shown in Fig. 4(b). To further investigate the field-effect behavior of the *p-i-n*-junction FET, we calculate the current density at a bias of –0.5 V under various gate voltages in the range of –10 to 10 V, as shown in Fig. 4(c). The figure shows that the effects of positive and negative gate voltages on the FET are symmetric, and the current increases with the gate voltage. The differential conductance (dI/dV) density of the *p-i-n*-junction FET under different gate voltages is calculated, as shown in the inset of Fig. 4(b). The figure shows that the dI/dV curve of the spin-down state almost equals zero over the entire bias range, and it exhibits full spin-polarized behavior. dI/dV of the spin-up state is 54.2 S/mm at a bias voltage of –0.5 V and gate voltage of 10 V, which is significantly larger than the maximum value of the *p-n* junction. At the positive-bias side, dI/dV of the spin-up state is almost zero under a gate voltage of 10 V, which is significantly smaller than the value under other gate voltages. This indicates that the *p-i-n*-junction FET shows excellent field-effect behavior and that the electric field can effectively enhance its unidirectional transport feature. The transmission performance and field-effect behavior of the *p-i-n*-junction transistor obtained by using PBE + *U* [see Fig. S3(b) within the Supplemental Material [69]] have similar characteristics to that obtained using PBE. In addition, from the spin-resolved transmission coefficient, $T(E)$, and PLDOSs shown in Figs. 4(d)–4(i) and the transmission spectra, $T(E, V)$, shown in Fig. S7 within the Supplemental Material [69], it can be seen that the *p-i-n*-junction FET has similar transport mechanisms to those of the *p-n*-junction diode.

D. Optical and photoelectric properties of the CrSCl monolayer and *p-i-n*-junction phototransistor

Furthermore, the optical properties and photoelectric performance of the CrSCl monolayer are investigated. The optical conductivity, complex refractive index, and absorption coefficient are calculated by [64]:

$$\sigma = -i\omega\epsilon_0\chi(\omega), n + ik = \sqrt{1 + i\frac{\sigma}{\epsilon_0\omega}}, \alpha = 2\frac{\omega}{c}\kappa, \quad (7)$$

where ω is an electromagnetic wave frequency, ϵ_0 is the electric constant, $\chi(\omega)$ is the susceptibility tensor, $\kappa(\omega)$ is the extinction coefficient, and c is the speed of light. The susceptibility tensor, $\chi(\omega)$, is determined from the Kubo-Greenwood formula [65]:

$$\chi_{ij}(\omega) = -\frac{e^2\hbar^4}{m^2\epsilon_0V\omega^2} \sum_{nm} \frac{f(E_m) - f(E_n)}{E_{mn} - \hbar\omega - i\Gamma} \pi_{nm}^i \pi_{nm}^j, \quad (8)$$

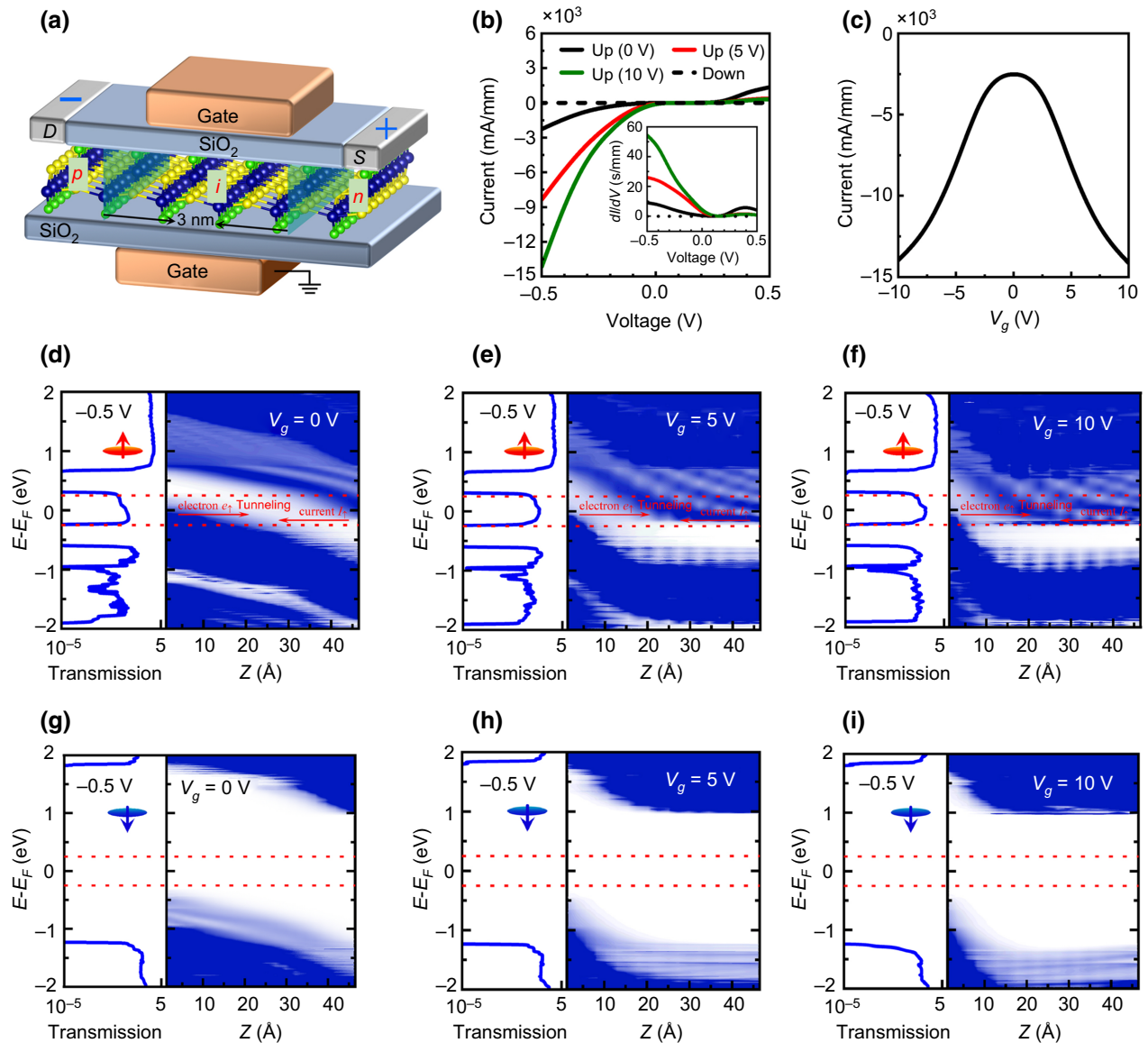


FIG. 4. Transport properties of the *p-i-n*-junction field-effect transistor of the 2D CrCl monolayer for a doping concentration of $3 \times 10^{13} \text{ cm}^{-2}$. (a) Schematic of *p-i-n*-junction field-effect transistor of the CrCl monolayer. (b) Bias-dependent current of the *p-i-n*-junction field-effect transistor under gate voltages of 0, 5, and 10 V, with the difference conductance curves shown in the inset. (c) Distribution of current at a bias of -0.5 V under different gate voltages. Spin-resolved transmission coefficient, $T(E)$, and PLDOS at a bias of -0.5 V under gate voltages of 0 V (d),(g), 5 V (e),(h), and 10 V (f),(i).

where V is the volume, f is the Fermi-Dirac function, Γ is the broadening, π_{nm}^i is the i th dipole matrix element between states n and m . The Γ value is generally selected to be between 0.01 and 0.1 eV. We use a default value of 0.086 eV in QuantumATK, corresponding to 1000 K. The absorption coefficients of the CrCl monolayer are calculated using the PBE functional, as shown in Fig. 5(a). It can be seen that the absorption edge begins at an energy of approximately 0.3 and 2.1 eV for the spin-up and -down states, respectively, which correspond to the band gaps of the spin-up and -down states, respectively. The absorption coefficient curves show two main peaks at around 1.0 and

3.6 eV for the spin-up states, and they show three main peaks at around 2.7, 3.6, and 4.2 eV for the spin-down states. It should be noted that the band gap is underestimated with the use of the PBE functional, which will influence the optical properties of a material. Therefore, we also calculate the optical properties using PBE + U , as shown in Fig. S8 within the Supplemental Material [69]. It indicates that the results obtained by the two methods are consistent with the overall contour, to some extent, but the position of the absorption edge and absorption peaks move to the high-energy region when considering the Hubbard U . The absorption regions of light for the

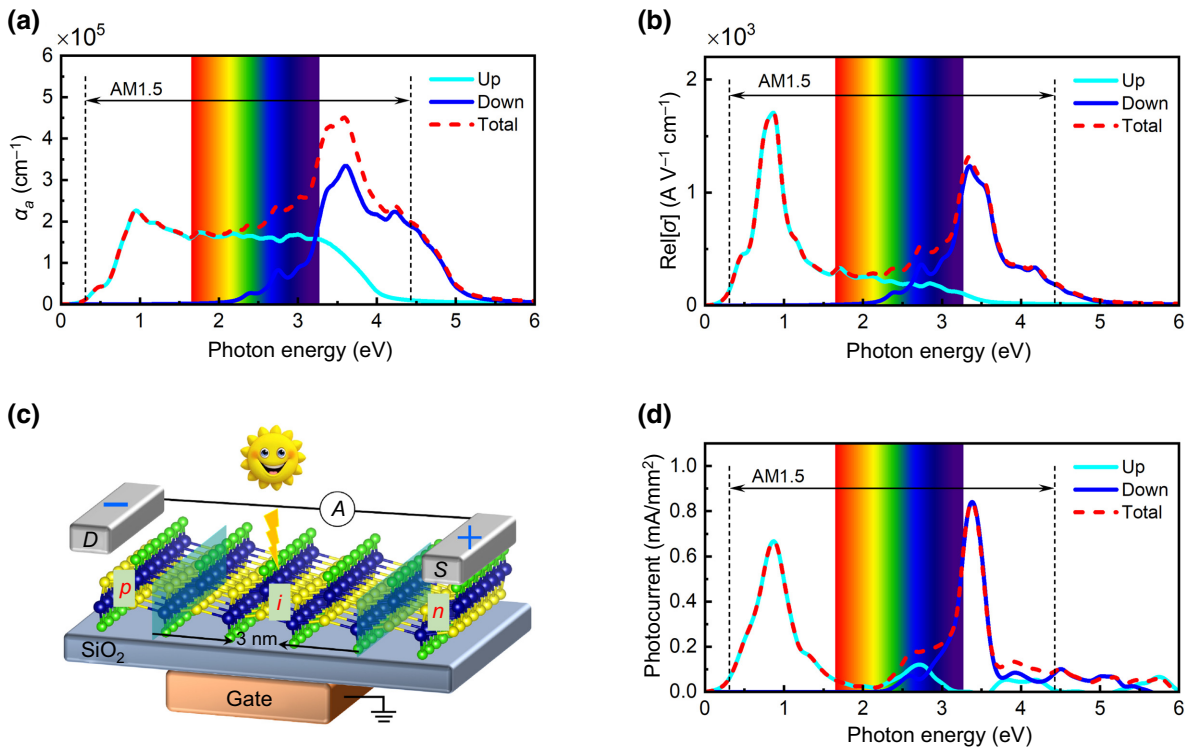


FIG. 5. Photoelectric properties of the 2D CrCl monolayer. Spin-resolved optical absorption coefficient (a) and optical conductivity (b) of the CrCl monolayer along the y direction. (c) Schematic of the p - i - n -junction phototransistor of the CrCl monolayer. (d) Spin-resolved photocurrent density of the p - i - n -junction phototransistor of the CrCl monolayer under zero bias for a doping concentration of $3 \times 10^{13} \text{ cm}^{-2}$. Embedded spectrum pattern in (a),(b),(d) displays visible-light region.

spin-up and -down states [see Fig. S8(a) within the Supplemental Material [69]] are completely separated in the low-energy region (visible region), which also results in similar behaviors of the optical conductivities and photocurrents in response to light, as shown in Figs. 5(b) and 5(d) and Figs. S8(b) and S8(c) within the Supplemental Material [69]. Both the optical absorption spectrum and optical conductivity of the spin-up states are in the spectral region within the AM1.5 standard [66]. Therefore, the CrCl monolayer is ideal for developing photovoltaic devices.

We further construct a phototransistor based on the p - i - n junction using the CrCl monolayer, as shown in Fig. 5(c), and we illustrate its photoresponse characteristics using linearly polarized light for optical excitation. The first-order correction to the photogenerated current at the electrode, $\alpha = D$ or S , due to the absorption of photons with frequency ω is given by [67,68]

$$I_\sigma = \frac{e}{\hbar} \int_{-\infty}^{\infty} \sum_{\beta=D,S} [1 - f_\alpha(E)] f_\beta(E - \hbar\omega) T_{\alpha,\beta}^-(E) - f_\alpha(E) [1 - f_\beta(E + \hbar\omega)] T_{\alpha,\beta}^+(E) dE. \quad (9)$$

The spin-resolved photocurrent density of a p - i - n -junction phototransistor for a doping concentration of $3 \times 10^{13} \text{ cm}^{-2}$

under zero bias (without power) is calculated using PBE and PBE + U , as shown in Figs. 5(d) and S8(c) within the Supplemental Material [69]. For the results of PBE, the spin-up photocurrent has a strong sharp peak of 0.7 mA/mm^2 at approximately 0.9 eV , and the spin-down photocurrent has a strong sharp peak of 0.9 mA/mm^2 at approximatively 3.4 eV . According to the results obtained by using PBE + U , the spin-up photocurrent peak is located in the yellow-light region, while the spin-down peak is located in the ultraviolet-light region. Therefore, the phototransistor's spin-up channel can be used for yellow-light detection, and the spin-down channel can be used for ultraviolet-light detection. In addition, the p - i - n -junction phototransistor can generate a fully spin-up polarized current in the visible range, which further indicates the potential for use in photoexcited spin-polarized electron-generation devices.

IV. SUMMARY

We investigate the electromagnetic properties of the CrCl monolayer and the spin-transport properties of p - n -junction diodes, field-effect transistors, and phototransistors. The results show that the CrCl monolayer possesses robust FM ordering, with a magnetic moment up to $3.288 \mu_B$ (PBE) per Cr atom and a high spin polarization.

Therefore, the *p-n*-junction diodes of the CrSCl monolayer show full spin-polarized transport behavior, and the transmission current can be manipulated through the doping concentration. The *p-i-n*-junction FET shows similar spin-filtering behavior to that of the *p-n*-junction diode, and the current density is dramatically enhanced at the negative-bias side as the gate voltage is applied. Furthermore, the optical properties and photoresponse characteristics of the phototransistor of the CrSCl monolayer indicate that the phototransistor's spin-up and -down channels can be used to detect different wavelengths of light, and the phototransistor can generate a fully spin-up polarized current in the visible range. The results provide a comprehensive description of various physical properties of the CrSCl monolayer, and they show the transition behavior and photoresponse characteristics of devices based on the CrSCl monolayer. These results demonstrate the potential applications of the CrSCl monolayer for high-performance spintronic and photovoltaic devices, and they call for further experimental verification and exploration for this material and related 2D materials.

ACKNOWLEDGMENTS

We acknowledge funding from the National Natural Science Foundation of China (Grants No. 12274117, No. 62274066, and No. 62275074), the Science Foundation for the Excellent Youth Scholars of Henan Province (Grant No. 202300410226), the Scientific and Technological Innovation Program of Henan Province's Universities (Grant No. 20HASTIT026), the Young Top-notch Talents Project of Henan Province (2021 year), and the Key Scientific Project of Universities of Henan Province (Grant No. 22A140020). We thank the High Performance Computing Center of Henan Normal University.

- [1] J. Wu, W. Pisula, and K. Müllen, Graphenes as potential material for electronics, *Chem. Rev.* **107**, 718 (2007).
- [2] M. Chhowalla, D. Jena, and H. Zhang, Two-dimensional semiconductors for transistors, *Nat. Rev. Mater.* **1**, 1 (2016).
- [3] R. Bian, C. Li, Q. Liu, G. Cao, Q. Fu, P. Meng, J. Zhou, F. Liu, and Z. Liu, Recent progress in the synthesis of novel two-dimensional van der Waals materials, *Natl. Sci. Rev.* **9**, nwab164 (2022).
- [4] Y. Deng, X. Liu, Y. Chen, Z. Du, N. Jiang, C. Shen, E. Zhang, H. Zheng, H.-Z. Lu, and K. Wang, All-electrical switching of a topological non-collinear antiferromagnet at room temperature, *Natl. Sci. Rev.* **10**, nwac154 (2023).
- [5] O. Lopez-Sanchez, D. Lembke, M. Kayci, A. Radenovic, and A. Kis, Ultrasensitive photodetectors based on monolayer MoS₂, *Nat. Nanotechnol.* **8**, 497 (2013).
- [6] Q. Yang, Z.-D. Luo, D. Zhang, M. Zhang, X. Gan, J. Seidel, Y. Liu, Y. Hao, and G. Han, Controlled optoelectronic response in van der Waals heterostructures for in-sensor computing, *Adv. Funct. Mater.* **32**, 202207290 (2022).
- [7] B. L. Li, J. Wang, H. L. Zou, S. Garaj, C. T. Lim, J. Xie, N. B. Li, and D. T. Leong, Low-dimensional transition metal dichalcogenide nanostructures based sensors, *Adv. Funct. Mater.* **26**, 7034 (2016).
- [8] Y. An, Y. Hou, K. Wang, S. Gong, C. Ma, C. Zhao, T. Wang, Z. Jiao, H. Wang, and R. Wu, Multifunctional lateral transition-metal disulfides heterojunctions, *Adv. Funct. Mater.* **30**, 2002939 (2020).
- [9] B. Radisavljevic, A. Radenovic, J. Brivio, V. Giacometti, and A. Kis, Single-layer MoS₂ transistors, *Nat. Nanotechnol.* **6**, 147 (2011).
- [10] L. Li, Y. Yu, G. J. Ye, Q. Ge, X. Ou, H. Wu, D. Feng, X. H. Chen, and Y. Zhang, Black phosphorus field-effect transistors, *Nat. Nanotechnol.* **9**, 372 (2014).
- [11] X. Li and X. Wu, Two-dimensional monolayer designs for spintronics applications, *WIREs Comput. Mol. Sci.* **6**, 441 (2016).
- [12] K. S. Novoselov, A. K. Geim, S. V. Morozov, D. Jiang, Y. Zhang, S. V. Dubonos, I. V. Grigorieva, and A. A. Firsov, Electric field effect in atomically thin carbon films, *Science* **306**, 666 (2004).
- [13] A. Loiseau, F. Willaime, N. Demonty, G. Hug, and H. Pascard, Boron Nitride Nanotubes with Reduced Numbers of Layers Synthesized by Arc Discharge, *Phys. Rev. Lett.* **76**, 4737 (1996).
- [14] H. Liu, Y. Du, Y. Deng, and P. D. Ye, Semiconducting black phosphorus: Synthesis, transport properties and electronic applications, *Chem. Soc. Rev.* **44**, 2732 (2015).
- [15] Y. Guo, S. Zhou, and J. Zhao, Two-dimensional intrinsic ferromagnets with high curie temperatures: Synthesis, physical properties and device applications, *J. Mater. Chem. C* **9**, 6103 (2021).
- [16] Y. Feng, N. Liu, and G. Gao, Spin transport properties in Dirac spin gapless semiconductors Cr₂X₃ with high Curie temperature and large magnetic anisotropic energy, *Appl. Phys. Lett.* **118**, 112407 (2021).
- [17] J. Yang, S. Fang, Y. Peng, S. Liu, B. Wu, R. Quhe, S. Ding, C. Yang, J. Ma, B. Shi, L. Xu, X. Sun, G. Tian, C. Wang, J. Shi, J. Lu, and J. Yang, Layer-Dependent Giant Magnetoresistance in Two-Dimensional CrPS₄ Magnetic Tunnel Junctions, *Phys. Rev. Appl.* **16**, 024011 (2021).
- [18] B. Huang, G. Clark, E. Navarro-Moratalla, D. R. Klein, R. Cheng, K. L. Seyler, D. Zhong, E. Schmidgall, M. A. McGuire, D. H. Cobden, W. Yao, D. Xiao, P. Jarillo-Herrero, and X. Xu, Layer-dependent ferromagnetism in a van der Waals crystal down to the monolayer limit, *Nature* **546**, 270 (2017).
- [19] M. Bonilla, S. Kolekar, Y. Ma, H. C. Diaz, V. Kalappattil, R. Das, T. Eggers, H. R. Gutierrez, M.-H. Phan, and M. Batzill, Strong room-temperature ferromagnetism in VSe₂ monolayers on van der Waals substrates, *Nat. Nanotechnol.* **13**, 289 (2018).
- [20] W. Yu, J. Li, T. S. Herng, Z. Wang, X. Zhao, X. Chi, W. Fu, I. Abdelwahab, J. Zhou, J. Dan, Z. Chen, Z. Chen, Z. Li, J. Lu, S. J. Pennycook, Y. P. Feng, J. Ding, and K. P. Loh, Chemically exfoliated VSe₂ monolayers with room-temperature ferromagnetism, *Adv. Mater.* **31**, 1903779 (2019).
- [21] C. Gong, L. Li, Z. Li, H. Ji, A. Stern, Y. Xia, T. Cao, W. Bao, C. Wang, Y. Wang, Z. Q. Qiu, R. J. Cava, S. G. Louie, J. Xia, and X. Zhang, Discovery of intrinsic ferromagnetism

- in two-dimensional van der Waals crystals, *Nature* **546**, 265 (2017).
- [22] Z. Hao, H. Li, S. Zhang, X. Li, G. Lin, X. Luo, Y. Sun, Z. Liu, and Y. Wang, Atomic scale electronic structure of the ferromagnetic semiconductor $\text{Cr}_2\text{Ge}_2\text{Te}_6$, *Sci. Bull.* **63**, 825 (2018).
- [23] V. Ostwal, T. Shen, and J. Appenzeller, Efficient spin-orbit torque switching of the semiconducting van der Waals ferromagnet $\text{Cr}_2\text{Ge}_2\text{Te}_6$, *Adv. Mater.* **32**, 1906021 (2020).
- [24] Y. Deng, Y. Yu, Y. Song, J. Zhang, N. Z. Wang, Z. Sun, Y. Yi, Y. Z. Wu, S. Wu, J. Zhu, J. Wang, X. H. Chen, and Y. Zhang, Gate-tunable room-temperature ferromagnetism in two-dimensional Fe_3GeTe_2 , *Nature* **563**, 94 (2018).
- [25] Z. Fei, B. Huang, P. Malinowski, W. Wang, T. Song, J. Sanchez, W. Yao, D. Xiao, X. Zhu, A. F. May, W. Wu, D. H. Cobden, J.-H. Chu, and X. Xu, Two-dimensional itinerant ferromagnetism in atomically thin Fe_3GeTe_2 , *Nat. Mater.* **17**, 778 (2018).
- [26] K. Zhang, S. Han, Y. Lee, M. J. Coak, J. Kim, I. Hwang, S. Son, J. Shin, M. Lim, D. Jo, K. Kim, D. Kim, H.-W. Lee, and J.-G. Park, Gigantic current control of coercive field and magnetic memory based on nanometer-thin ferromagnetic van der Waals Fe_3GeTe_2 , *Adv. Mater.* **33**, 2004110 (2021).
- [27] J. Li, Y. Li, S. Du, Z. Wang, B.-L. Gu, S.-C. Zhang, K. He, W. Duan, and Y. Xu, Intrinsic magnetic topological insulators in van der Waals layered MnBi_2Te_4 -family materials, *Sci. Adv.* **5**, eaaw5685 (2019).
- [28] Y. Deng, Y. Yu, M. Z. Shi, Z. Guo, Z. Xu, J. Wang, X. H. Chen, and Y. Zhang, Quantum anomalous Hall effect in intrinsic magnetic topological insulator MnBi_2Te_4 , *Science* **367**, 895 (2020).
- [29] Y. Yuan, X. Wang, H. Li, J. Li, Y. Ji, Z. Hao, Y. Wu, K. He, Y. Wang, Y. Xu, W. Duan, W. Li, and Q.-K. Xue, Electronic states and magnetic response of MnBi_2Te_4 by scanning tunneling microscopy and spectroscopy, *Nano Lett.* **20**, 3271 (2020).
- [30] Y. An, K. Wang, S. Gong, Y. Hou, C. Ma, M. Zhu, C. Zhao, T. Wang, S. Ma, H. Wang, R. Wu, and W. Liu, Nanodevices engineering and spin transport properties of MnBi_2Te_4 monolayer, *npj Comput. Mater.* **7**, 1 (2021).
- [31] N. Miao, B. Xu, L. Zhu, J. Zhou, and Z. Sun, 2D intrinsic ferromagnets from van der Waals antiferromagnets, *J. Am. Chem. Soc.* **140**, 2417 (2018).
- [32] Z. Jiang, P. Wang, J. Xing, X. Jiang, and J. Zhao, Screening and design of novel 2D ferromagnetic materials with high Curie temperature above room temperature, *ACS Appl. Mater. Interfaces* **10**, 39032 (2018).
- [33] C. Wang, X. Zhou, L. Zhou, N.-H. Tong, Z.-Y. Lu, and W. Ji, A family of high-temperature ferromagnetic monolayers with locked spin-dichroism-mobility anisotropy: MnNX and CrCX ($X = \text{Cl}, \text{Br}, \text{I}; C = \text{AS}, \text{Se}, \text{Te}$), *Sci. Bull.* **64**, 293 (2019).
- [34] E. J. Telford, *et al.*, Coupling between magnetic order and charge transport in a two-dimensional magnetic semiconductor, *Nat. Mater.* **21**, 754 (2022).
- [35] A. N. Christensen, T. Johansson, and S. Quézel, Preparation and magnetic properties of CrOCl , *Acta Chem. Scand.* **28**, 1171 (1974).
- [36] F. Kanamaru, S. Yamanaka, M. Koizumi, and S. Nagai, Synthesis and some properties of a layer-type inorganic-organic complex of FeOCl and pyridine, *Chem. Lett.* **3**, 373 (1974).
- [37] M. Wang, J. Zhang, Z. Wang, C. Wang, S. van Smaalen, H. Xiao, X. Chen, C. Du, X. Xu, and X. Tao, Broadband CrOCl saturable absorber with a spectral region extension to $10.6\ \mu\text{m}$, *Adv. Opt. Mater.* **8**, 1901446 (2020).
- [38] T. Zhang, Y. Wang, H. Li, F. Zhong, J. Shi, M. Wu, Z. Sun, W. Shen, B. Wei, W. Hu, X. Liu, L. Huang, C. Hu, Z. Wang, C. Jiang, S. Yang, Q.-M. Zhang, and Z. Qu, Magnetism and optical anisotropy in van der Waals antiferromagnetic insulator CrOCl , *ACS Nano* **13**, 11353 (2019).
- [39] E. J. Telford, A. H. Dismukes, K. Lee, M. Cheng, A. Wieteska, A. K. Bartholomew, Y.-S. Chen, X. Xu, A. N. Pasupathy, X. Zhu, C. R. Dean, and X. Roy, Layered antiferromagnetism induces large negative magnetoresistance in the van der Waals semiconductor CrSBr , *Adv. Mater.* **32**, 2003240 (2020).
- [40] Y. Guo, Y. Zhang, S. Yuan, B. Wang, and J. Wang, Chromium sulfide halide monolayers: Intrinsic ferromagnetic semiconductors with large spin polarization and high carrier mobility, *Nanoscale* **10**, 18036 (2018).
- [41] R. Zacharia, H. Ulbricht, and T. Hertel, Interlayer cohesive energy of graphite from thermal desorption of polyaromatic hydrocarbons, *Phys. Rev. B* **69**, 155406 (2004).
- [42] J. Taylor, H. Guo, and J. Wang, *Ab initio* modeling of open systems: Charge transfer, electron conduction, and molecular switching of a C_{60} device, *Phys. Rev. B* **63**, 121104 (2001).
- [43] M. Brandbyge, J.-L. Mozos, P. Ordejón, J. Taylor, and K. Stokbro, Density-functional method for nonequilibrium electron transport, *Phys. Rev. B* **65**, 165401 (2002).
- [44] J. M. Soler, E. Artacho, J. D. Gale, A. García, J. Junquera, P. Ordejón, and D. Sánchez-Portal, The SIESTA method for *ab initio* order- N materials simulation, *J. Phys.: Condens. Matter* **14**, 2745 (2002).
- [45] J. P. Perdew, K. Burke, and M. Ernzerhof, Generalized Gradient Approximation Made Simple, *Phys. Rev. Lett.* **77**, 3865 (1996).
- [46] A. Mogulkoc, M. Modarresi, and A. N. Rudenko, Two-dimensional chromium pnictides $\text{Cr}X$ ($X = \text{P}, \text{As}, \text{Sb}$): Half-metallic ferromagnets with high Curie temperature, *Phys. Rev. B* **102**, 024441 (2020).
- [47] A. Mogulkoc, M. Modarresi, and A. N. Rudenko, Two-Dimensional Chromium Bismuthate: A Room-Temperature Ising Ferromagnet with Tunable Magneto-Optical Response, *Phys. Rev. Appl.* **15**, 064053 (2021).
- [48] R. Caglayan, Y. Mogulkoc, A. Mogulkoc, M. Modarresi, and A. N. Rudenko, Easy-axis rotation in ferromagnetic monolayer CrN induced by fluorine and chlorine functionalization, *Phys. Chem. Chem. Phys.* **24**, 25426 (2022).
- [49] D. R. Hamann, Optimized norm-conserving Vanderbilt pseudopotentials, *Phys. Rev. B* **88**, 085117 (2013).
- [50] M. Schlipf and F. Gygi, Optimization algorithm for the generation of ONCV pseudopotentials, *Comput. Phys. Commun.* **196**, 36 (2015).
- [51] J. Heyd, G. E. Scuseria, and M. Ernzerhof, Hybrid functionals based on a screened coulomb potential, *J. Chem. Phys.* **118**, 8207 (2003).

- [52] H. J. Monkhorst and J. D. Pack, Special points for Brillouin-zone integrations, *Phys. Rev. B* **13**, 5188 (1976).
- [53] M. Pajda, J. Kudrnovský, I. Turek, V. Drchal, and P. Bruno, *Ab initio* calculations of exchange interactions, spin-wave stiffness constants, and Curie temperatures of Fe, Co, and Ni, *Phys. Rev. B* **64**, 174402 (2001).
- [54] B. Xu, S. Li, K. Jiang, J. Yin, Z. Liu, Y. Cheng, and W. Zhong, Switching of the magnetic anisotropy via strain in two dimensional multiferroic materials: CrSX ($X = \text{Cl}, \text{Br}, \text{I}$), *Appl. Phys. Lett.* **116**, 052403 (2020).
- [55] J. L. Lado and J. Fernández-Rossier, On the origin of magnetic anisotropy in two dimensional CrI₃, *2D Mater.* **4**, 035002 (2017).
- [56] G. Daalderop, P. Kelly, and M. Schuurmans, First-principles calculation of the magnetocrystalline anisotropy energy of iron, cobalt, and nickel, *Phys. Rev. B* **41**, 11919 (1990).
- [57] D. Stradi, U. Martinez, A. Blom, M. Brandbyge, and K. Stokbro, General atomistic approach for modeling metal-semiconductor interfaces using density functional theory and nonequilibrium Green's function, *Phys. Rev. B* **93**, 155302 (2016).
- [58] T. Gunst, T. Markussen, M. L. N. Palsgaard, K. Stokbro, and M. Brandbyge, First-principles electron transport with phonon coupling: Large scale at low cost, *Phys. Rev. B* **96**, 161404 (2017).
- [59] M. Büttiker, Y. Imry, R. Landauer, and S. Pinhas, Generalized many-channel conductance formula with application to small rings, *Phys. Rev. B* **31**, 6207 (1985).
- [60] Y. An, M. Zhang, D. Wu, T. Wang, Z. Jiao, C. Xia, Z. Fu, and K. Wang, The rectifying and negative differential resistance effects in graphene/h-BN nanoribbon heterojunctions, *Phys. Chem. Chem. Phys.* **18**, 27976 (2016).
- [61] V. Zatko, M. Galbiati, S. M.-M. Dubois, M. Och, P. Palczynski, C. Mattevi, P. Brus, O. Bezencenet, M.-B. Martin, B. Servet, J.-C. Charlier, F. Godel, A. Vecchiola, K. Bouzehouane, S. Collin, F. Petroff, B. Dlubak, and P. Seneor, Band-structure spin-filtering in vertical spin valves based on chemical vapor deposited WS₂, *ACS Nano* **13**, 14468 (2019).
- [62] Y. Zheng, X. Ma, F. Yan, H. Lin, W. Zhu, Y. Ji, R. Wang, and K. Wang, Spin filtering effect in all-van der Waals heterostructures with WSe₂ barriers, *npj 2D Mater. Appl.* **6**, 62 (2022).
- [63] S. Ahmed, X. Ding, P. P. Murmu, N. N. Bao, R. Liu, J. Kennedy, J. Ding, and J. B. Yi, Magnetic properties of Co doped WSe₂ by implantation, *J. Alloys Compd.* **731**, 25 (2018).
- [64] R. M. Martin, *Electronic structure: Basic theory and practical methods* (Cambridge University Press, Cambridge, 2004).
- [65] J. E. Sipe and E. Ghahramani, Nonlinear optical response of semiconductors in the independent-particle approximation, *Phys. Rev. B* **48**, 11705 (1993).
- [66] G. ASTM, 173-03, in Terrestrial reference spectra for photovoltaic performance evaluation (American Society for Testing Materials (ASTM) International: West Conshohocken, 2012).
- [67] M. Palsgaard, T. Markussen, T. Gunst, M. Brandbyge, and K. Stokbro, Efficient First-Principles Calculation of Phonon-Assisted Photocurrent in Large-Scale Solar-Cell Devices, *Phys. Rev. Appl.* **10**, 014026 (2018).
- [68] L. Zhang, K. Gong, J. Chen, L. Liu, Y. Zhu, D. Xiao, and H. Guo, Generation and transport of valley-polarized current in transition-metal dichalcogenides, *Phys. Rev. B* **90**, 195428 (2014).
- [69] See the Supplemental Material at <http://link.aps.org-supplemental/10.1103/PhysRevApplied.19.054013> for supplemental Figs. S1–S8.